eScience 2 (2022) 655–665

Contents lists available at ScienceDirect

eScience

journal homepage: www.keaipublishing.com/en/journals/escience

Research Paper

Highly aligned lithiophilic electrospun nanofiber membrane for the multiscale suppression of Li dendrite growth

Jianan Wang [a,c], Qianyue Ma [a], Shiyi Sun [a], Kai Yang [c], Qiong Cai [c], Emilia Olsson [e,f], Xin Chen [a], Ze Wang [a], Amr M. Abdelkader [g], Yinshi Li [d], Wei Yan [a,*], Shujiang Ding [b,*], Kai Xi [b,*]

[a] Department of Environmental Science and Engineering, Xi'an Key Laboratory of Solid Waste Recycling and Resource Recovery, School of Energy and Power Engineering, Xi'an Jiaotong University, Xi'an 710049, China
[b] Department of Applied Chemistry, School of Chemistry, University Engineering Research Center of Energy Storage Materials and Chemistry of Shaanxi Province, State Key Laboratory for Electrical Insulation and Power Equipment, Xi'an Jiaotong University, Xi'an 710049, China
[c] Department of Chemical and Process Engineering, Faculty of Engineering and Physical Sciences, Advanced Technology Institute, University of Surrey, Guildford GU2 7XH, Surrey, England, UK
[d] Key Laboratory of Thermo-Fluid Science and Engineering of Ministry of Education, School of Energy and Power Engineering, Xi'an Jiaotong University, Xi'an, Shaanxi, 710049, China
[e] Advanced Research Center for Nanolithography, Science Park 106, 1098 XG, Amsterdam, the Netherlands
[f] Institute of Physics and Institute for Theoretical Physics, University of Amsterdam, Postbus 94485, 1090 GL, Amsterdam, the Netherlands
[g] Faculty of Science and Technology, Bournemouth University, Talbot Campus, Fern Barrow, Poole, England, BH12 5BB, UK

HIGHLIGHTS

- A highly aligned lithiophilic TiO_2/SiO_2 (A-TS) electrospun nanofiber membrane is developed.
- A custom-made electrospinning system is introduced to control the orientation of the fibers in the membrane.
- Suppressing dendrite growth at both membrane and fiber scales to achieve excellent cycling performance in various batteries.

GRAPHICAL ABSTRACT

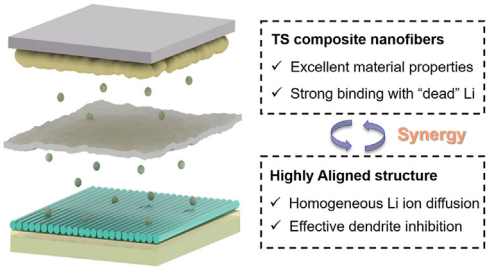

ARTICLE INFO

Keywords:
Aligned structure
Protective layer
Li dendrite
Lithium sulfur battery
Li metal battery

ABSTRACT

Using inorganic fibrous membranes as protective layers has yielded success in suppressing dendrite growth. However, conventional fibrous membranes usually have large voids and low affinity for Li, promoting inhomogeneous charge distribution and allowing some dendrites to grow. Herein, we introduce a highly aligned TiO_2/SiO_2 (A-TS) electrospun nanofiber membrane as a protective layer for the Li metal anode. The A-TS membrane is fabricated by a custom-made electrospinning system with an automatic fiber alignment collector that allows control of the fibers' orientation. At the scale of the individual fibers, their high binding energies with Li can attract more "dead" Li by reacting with the SiO_2 component of the composite, avoiding uncontrollable deposition on the metal anode. At the membrane scale, these highly ordered structures achieve homogeneous contact and charge distribution on the Li metal surface, leaving no vulnerable areas to nucleate dendrite formation. Additionally, the excellent mechanical and thermal stability properties of the A-TS membrane prevent any potential puncturing by dendrites or thermal runaway in a battery. Hence, an A-TS@Li anode exhibits stable cycling performance when used in both Li–S and Li–NCM811 batteries, highlighting significant reference values for the future design and development of high-energy-density metal-based battery systems.

* Corresponding authors.
E-mail addresses: yanwei@xjtu.edu.cn (W. Yan), dingsj@xjtu.edu.cn (S. Ding), kx210.cam@xjtu.edu.cn (K. Xi).

https://doi.org/10.1016/j.esci.2022.09.001
Received 18 May 2022; Received in revised form 23 August 2022; Accepted 2 September 2022
Available online 11 September 2022

1. Introduction

In recent years, there has been an increasing demand for safe high-energy Li batteries for electric grids, portable electronics, and electric vehicles [1,2,3,4]. Li metal is regarded as the most attractive anode material in Li-based batteries due to its ultrahigh theoretical specific capacity of 3860 mAh g^{-1} (compared with 372 mAh g^{-1} for a graphite anode) and low redox potential (−3.04 V versus a standard hydrogen electrode) [5,6,7,8]. In addition, Li metal anodes can be matched with various cathodes (e.g., sulfur, oxygen, $LiCoO_2$, $LiFePO_4$, $LiNi_xMn_yCo_zO_2$) in some promising high-energy batteries, such as lithium–sulfur and lithium–air.

Despite the advantages of the Li metal anode, there are still serious challenges that need to be overcome before it can achieve its full potential. The uncontrollable growth of Li dendrites resulting from inhomogeneous charge distribution on the anode surface is at the top of the challenge list. Li dendrites can break the solid electrolyte interphase (SEI) layer and accelerate the consumption of organic electrolytes, decreasing the Coulombic efficiency and cycle life [9,10,11]. In addition, dendrites can penetrate the separator and consequently short-circuit the cell, potentially creating safety hazards [12,13,14].

Several concepts have been suggested to tackle the dendrite growth problem, including deploying a three-dimensional (3D) conductive skeleton to accommodate Li protrusion, designing a functional separator facing the Li side, preforming a protective SEI layer on the Li metal, and others [15,16,17,18]. Among these, constructing an artificial interlayer between the separator and the Li anode is reported to stabilize the SEI layer and regulate Li^+ deposition [19,20,21,22]. In this regard, a 3D porous structure based on continuous nanofibers or electrospun nanofiber membranes demonstrated great success when used as an artificial protective layer [23,24,25,26,27]. The abundant volume available in the porous structure, combined with its high mechanical flexibility, allows it to accommodate the significant volumetric change that the Li metal anode undergoes during repeated deposition and stripping [28,29]. Further, the large specific surface area facilitates the processes at the electrolyte/Li interface, extending the Sand's time and ensuring a stable and homogeneous Li^+ flux. It is also possible to improve the separator and anode wettability and other physicochemical properties by inducing some functionality on the nanofiber membranes, further suppressing the growth of Li dendrites. In addition, the electrospinning technique is cheap and industrially mature, enabling large-scale fabrication and commercialization [29].

Despite the enhancement of anode stability when a nanofibrous protective layer is used, there are still issues that need to be addressed before practical applications can be considered. The random spatial orientation of conventional electrospun nanofibers can lead to large voids within the membrane that allow the growth of Li dendrites [30]. Most previous studies in the literature have used a carbon-based nanofibrous protective layer as the membrane skeleton, owing to the high electrical conductivity and promising Li storage ability of carbon materials (e.g., hard carbon and graphite) [26,31,32,33,34]. However, the Li affinity of some carbon materials is lower than that of elementary metal substances (e.g., Ag, Si, and Mg) and metal oxides (e.g., Al_2O_3, TiO_2, ZnO, and SiO_2), and they have a low Li nucleation energy barrier [33,35,36], originating from a lattice mismatch between the body-centered cubic (bcc) lithium structure and the hexagonal carbon structure [37]. Although some "lithiophilic" metal sulfides (MoS_2, ZnS, and VS_2) were recently used as an artificial interlayer to improve Li nucleation via electrochemical conversion between the metal sulfides and Li [38,39,40], their large-scale production is hindered by synthetic complexity, environmental instability, and high cost. Therefore, the design of a protective layer with high chemical stability, uniform pore size distribution, and lithiophilic materials may bring a breath of fresh air to the design of high-performance Li anodes.

Herein, we propose a highly aligned TiO_2/SiO_2 (A-TS) electrospun nanofiber membrane to serve as a protective layer for the Li metal anode. We also introduce a custom-made electrospinning system with an automatic fiber alignment collection device to prepare the inorganic membranes. At the membrane scale, the well-arranged nanofibrous array structure of the A-TS membrane guarantees homogeneous charge distribution and fast Li^+ diffusion. The membrane also provides room to accommodate any dendrites formed and, together with the mechanically strong fibers, significantly minimizes the chance of short-circuiting. At the fiber scale, the "lithiophilic" inorganic ceramics (TiO_2 and SiO_2) chemically bind/react with "dead" Li to further suppress dendrite growth and achieve the efficient deposition and stripping of Li. As a result, the designed A-TS membrane supports the Li metal anode to achieve outstanding cycling and rate capability performance that outshines most Li metal anodes in the literature, including those using nanofiber membranes.

2. Results and discussion

Fig. 1 shows schematic illustrations of Li metal batteries with bare Li foil, C-TS@Li, and A-TS@Li anodes. Compared with bare Li, where Li dendrite growth is fast and uncontrollable (Fig. 1a) [41,42], the lithiophilic TS electrospun nanofiber membrane inhibits uncontrolled dendrite growth and provides physical space to accommodate any formed dendrites. However, due to the inherent bending instability effect of the jet in conventional electrospinning systems, the C-TS membrane is inevitably composed of randomly arranged nanofibers (Fig. 1b) [30,43]. As a result, the as-spun C-TS membrane retains plenty of large voids, and the charge diffusion is slightly inhomogeneous.

Highly aligned A-TS electrospun nanofiber membranes can regulate the charge distribution and further improve the ability to inhibit Li dendrites. The A-TS membrane is prepared using a custom-designed electrospinning system consisting of two parallel electrodes and one additional assistant electrode (Fig. 1b). An electric reciprocating mechanical arm driven by digital pulse power is also added into this electrospinning configuration, aiming to realize the fully automated and large-scale production of highly aligned fibers. More details and photos of the working mechanism of the custom-designed electrospinning configuration are shown in Fig. S1. The densely and highly ordered fiber-stacked structure of the A-TS membrane, combined with the excellent physical/chemical properties of the TiO_2/SiO_2 fibers, promotes more effective suppression of Li dendrites and enhances the cycling performance of Li metal batteries.

We first investigated the optimum conditions to obtain a robust, free-standing electrospun nanofiber membrane of C-TS and A-TS (as shown in Figs. S2–4). Pure TiO_2 electrospun nanofibers are too fragile to form free-standing membranes. TiO_2/SiO_2 electrospun composite membranes, on the other hand, can achieve excellent mechanical strength/flexibility with optimal material properties when calcined at 500 °C. Thermogravimetric analysis (TGA) demonstrated that the organic compounds from the precursors were entirely removed at 500 °C to form inorganic C-TS and A-TS nanofibers (Fig. S5). Hence, the C-TS and A-TS membranes were fabricated and then calcined at 500 °C to serve as a protective layer for the Li metal anode. It should be mentioned here that the average diameters of the C-TS and A-TS nanofibers were almost the same, 303.2 nm and 306.6 nm, respectively, despite changes in the electrospinning configuration (Figs. 2a–c and Figs. S2 and S6).

The formation of homogeneous TS nanofibers in both C-TS and A-TS was proven by EDS elemental mapping and XPS analysis, as can be seen in Figs. 2g–i and Fig. S7. According to the TEM and XRD analyses shown in Figs. 2d–h and Figs. S6c–e, the C-TS and A-TS nanofibers possessed lower crystallinity than the C-T nanofibers calcined under the same conditions. Unlike the clear crystalline structure of the C-T nanofibers, as presented in their SAED and XRD patterns, only one weak diffraction ring and a shallow peak corresponding to the (101) plane of anatase TiO_2 (JCPDS No. 21–1272) were observed in the traces of C-TS and A-TS.

These results suggest the amorphous SiO_2 phase introduced in the TS nanofibers retarded the long-order growth of the original TiO_2 crystals [44]. The low crystallinity of TiO_2 and SiO_2 improved the affinity of the fibers toward Li and thus guided uniform Li nucleation [35]. The addition of SiO_2 to the TiO_2 seems to have given the protective layer another advantage with respect to enhancing the Li anode performance. As can be seen from Fig. 2j and Fig. S8, the N_2 adsorption–desorption isotherms suggest an over four-fold increase in the BET specific surface area in the composite fibers compared to C-T, without influencing the intrinsic pore size distribution; this is mainly attributed to the introduced amorphous SiO_2 phase, which increased the surface area of the original TiO_2 nanofibers [45,46]. The higher surface area of the protective layer guaranteed more active sites and room to react with and deposit "dead" Li, thereby alleviating the issue of dendrite penetration [47,48].

The protective layer's mechanical and thermal stability properties are important for increasing battery life and ensuring safe operation. As shown in Fig. 3, the composite TS nanofibers and the highly aligned fiber-stacked structure demonstrated high mechanical strength when attached to the separator. A PP separator with an A-TS membrane exhibited the highest puncture resistance compared with both a pure PP separator and a separator reinforced with a C-TS membrane, implying the protected separator's stronger ability to physically resist being punctured by the Li dendrites (Figs. 3a and b and Fig. S9). The high mechanical stability of TiO_2 and the fiber-stacked structure of the A-TS membrane also minimized potential volume change in the SiO_2 and Si after lithiation [49,50]. The thermal stability and flame retardancy of the inorganic TiO_2/SiO_2 membrane was much higher than that of the commercial PP separator. While the PP separator instantly caught fire upon exposure to flame, the TS membranes showed significant resistance and maintained their original shape after over a minute of exposure to direct flame (Fig. 3c and d). The nonflammability and higher thermal resistance of this protective layer thus will increase battery safety by impeding heat diffusion if the PP separator shrinks and thermal runaway happens.

The binding energies of anatase TiO_2, amorphous SiO_2, and graphene towards Li atoms were further calculated using density functional theory (DFT) to evaluate their lithiophilic features. As shown in Figs. 3e, the binding energies of a Li atom on the TiO_2 (101) surface and on amorphous SiO_2 can reach up to −2.07 and −1.86 eV, respectively, much stronger than on graphene (−0.91 eV), proving the high chemical affinity of both anatase TiO_2 and amorphous SiO_2 toward Li. Low Li affinity will lead to inhomogeneous Li^+ flux and easily give rise to uneven Li nucleation, resulting in a loose Li interphase and lower cyclability for the Li anode, especially under high current densities [37,51]. In contrast, as the nucleation and deposition of Li preferentially happen on the surface of polar metals or metal oxides, TiO_2 and SiO_2 have stronger binding energies with Li and show better lithiophilicity [52,53].

According to previous reports, the lithiation mechanism of TiO_2 and SiO_2 can be explained by the following steps [54,55]:

$$TiO_2 + Li^+ + e^- \rightarrow LiTiO_2 \quad (1)$$

$$5SiO_2 + 4Li^+ + 4e^- \rightarrow 2Li_2Si_2O_5 + Si \quad (2)$$

$$2SiO_2 + 4Li^+ + 4e^- \rightarrow Li_4SiO_4 + Si \quad (3)$$

$$4Si + 15Li^+ + 15e^- \rightarrow Li_{15}Si_4 \quad (4)$$

Based on steps (2), (3), and (4), the presence of amorphous SiO_2 enables the activation of more "dead" Li, based on its specific alloying reaction mechanism and low energy barriers; in addition, it enhances the mechanical flexibility of the free-standing membrane. The formation of the intermediate Li silicate phases and the Li–Si alloy were proven by the subsequent XPS analysis presented in Fig. 6g [54,56]. Meanwhile, according to equation (1), the anatase TiO_2 contained in

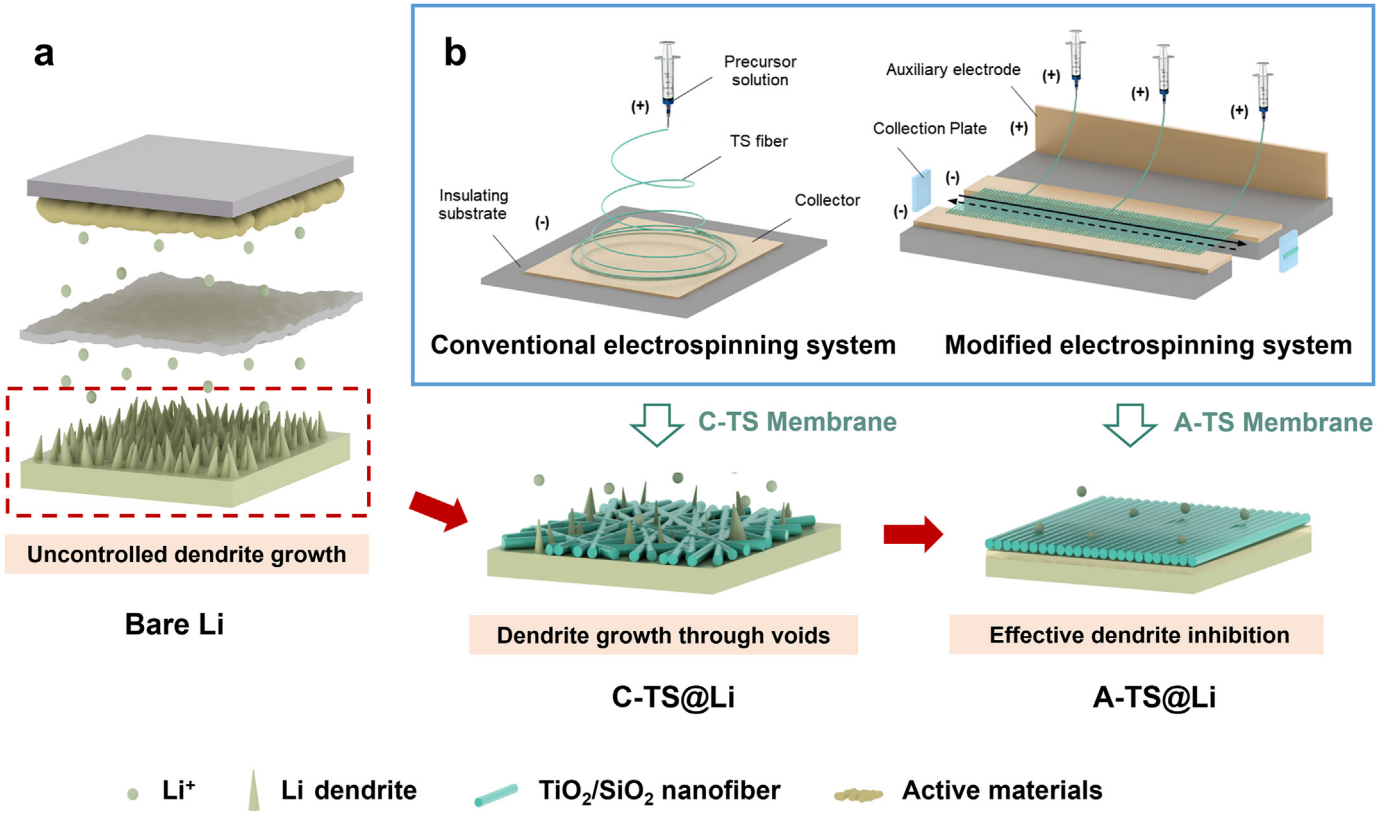

Fig. 1. (a) Schematic illustrations of Li metal batteries with bare Li, C-TS@Li, and A-TS@Li anodes; (b) conventional electrospinning system for the fabrication of C-TS electrospun nanofiber membrane, and the self-designed modified electrospinning system used to fabricate the A-TS electrospun nanofiber membrane.

TS fibers can not only stabilize the volume change experienced by SiO_2 and Si after lithiation but also provide intercalation space to accommodate and react with Li [53,55]. After the initial lithiation process, all the Li-containing compounds served as efficient Li ionic conductors to ensure a higher Li^+ transfer rate. In addition, owing to its aligned porous structure and high electrolyte affinity, the A-TS membrane also exhibited much smaller contact angles with different electrolytes, suggesting faster Li^+ diffusion would be achieved in various electrolyte systems (Fig. S10).

The interaction between deposited Li and TS nanofiber is illustrated in Fig. 3f. During battery cycling, the high chemical affinity between the TS nanofiber and Li drives a strong binding force to anchor nonactivated Li, slowing down the vertical growth of Li dendrites. More adsorbed Li^+ reacts with the amorphous SiO_2 to form lithiophilic Li-containing compounds based on the alloying reaction mechanism, and the Li-containing compounds further provide more sites to adsorb Li^+ and facilitate Li^+ diffusion [35,54]. Therefore, the deposition and plating behaviors of Li are stabilized under the protection of the TS membrane. This mechanism was proven experimentally using Li–TiO_2 and Li–TiO_2/SiO_2 batteries assembled with a TiO_2 or TiO_2/SiO_2 cathode and a Li metal anode (details on the cell assembly are in the Experimental section in the Supporting Information). A sufficient Li source enabled Li ions to fully embed into the TiO_2 or TS electrospun nanofibers in every cycle in the tested battery system. After 400 embedding/de-embedding cycles (Figs. 3g and h), the SEM images show that the pure TiO_2 nanofibers still had a relatively smooth surface with no obvious anchoring effect; in contrast, the TS composite fibers were almost covered with anchored Li-containing nanoparticles. In addition, the TS nanofibers presented a nearly 1.5 times higher capacity during the Li^+ embedding process than the pure TiO_2 nanofibers at all cycles (Fig. 3i). These results confirmed the role of the amorphous SiO_2 phase in the continuous anchoring and conversion of "dead" Li.

The membrane-scale advantages of the A-TS membrane for the suppression of Li dendrite growth are further investigated in Fig. 4. A bare Li anode without a protective layer had difficulty avoiding Li dendrite growth and the volumetric change Li metal undergoes during repeated deposition/stripping processes [16,57,58]. The unevenly distributed charges also induced the Li^+ to aggregate near the dendrites, thereby accelerating the uncontrollable growth of dendrites, resulting in severe electrolyte consumption and the fragmentation of the SEI layer [9,16]. Hence, the surface of the bare Li anode after cycling was quite rough, with plenty of micron-sized dendrites growing out of control over the whole anode

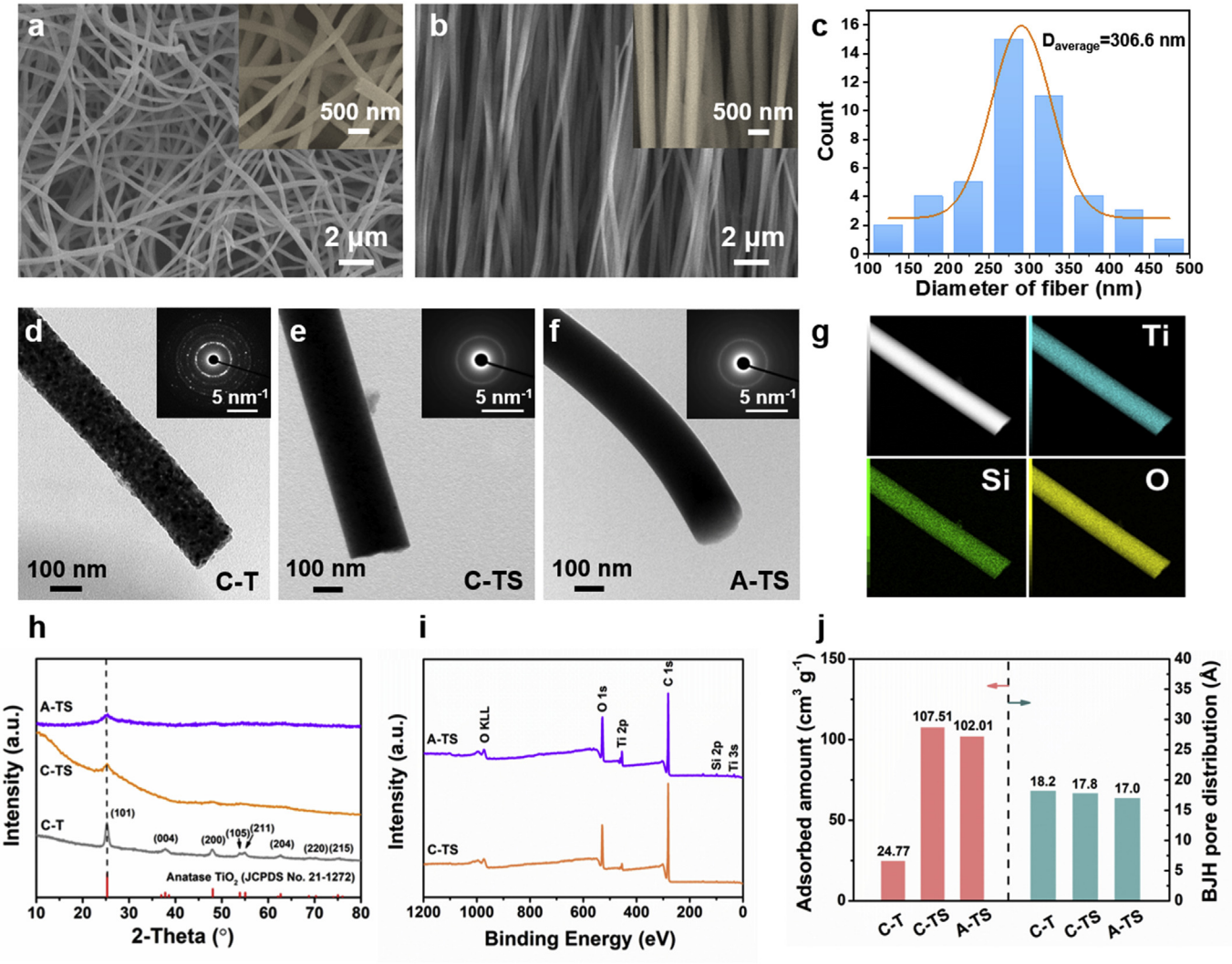

Fig. 2. Morphological and structural characterizations of various samples. Field emission scanning electron microscopy (FE-SEM) images of (a) C-TS and (b) A-TS membranes; (c) the diameter distribution of A-TS nanofibers measured from the membrane in Fig. 2b; (d–f) transmission electron microscopy (TEM) images of C-T, C-TS, and A-TS nanofibers; the inset is the selective area electron diffraction (SAED) pattern; (g) energy-dispersive spectrometer (EDS) mapping of the A-TS nanofiber; (h) X-ray diffraction (XRD) patterns of C-T, C-TS, and A-TS nanofibers; (i) X-ray photoelectron spectroscopy (XPS) fully scanned spectra of C-TS and A-TS nanofibers; (j) comparisons of Brunauer–Emmett–Teller (BET) specific surface area and BJH average pore size for C-T, C-TS, and A-TS nanofibers.

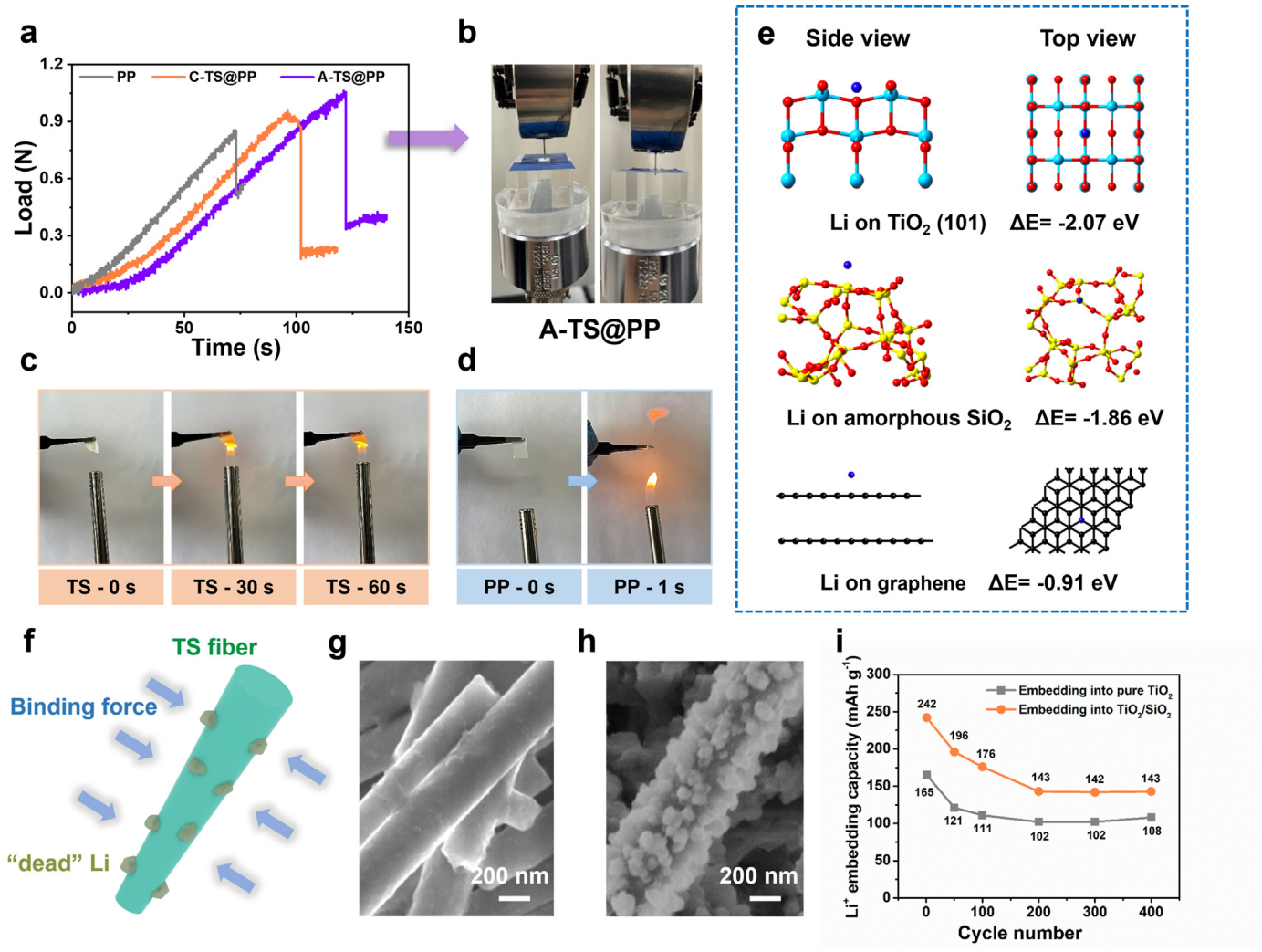

Fig. 3. (a) The puncture strength curves of the PP, C-TS@PP, and A-TS@PP membranes; (b) real photos before and after the mechanical puncture test for the A-TS@PP membrane; flame-retardant tests of the (c) TS membrane and (d) PP separator; (e) density functional theory calculation of the binding energies of a Li atom on the anatase TiO_2 (101) surface, amorphous SiO_2, and carbon (conducted using the Vienna Ab initio Simulation Package (VASP)); (f) schematic illustrations of the TS nanofiber binding with Li ions and adsorbing "dead" Li during cycling; Li^+ binding ability measurements in the Li–TiO_2 and Li–TiO_2/SiO_2 batteries (voltage range: 0.01–3 V vs. Li/Li^+; current: 400 mA g^{-1}); FE-SEM images of the (g) pure TiO_2 nanofiber and (h) TS nanofiber after 400 cycles, and (i) the Li^+ embedding capacities after different cycles.

surface (Figs. 4a and d). With the C-TS@Li anode, Li dendrite growth was alleviated to a certain extent. However, some small dendrites were still observed, mainly due to the uneven charge distribution and some large voids in the C-TS membrane (Figs. 4b and e). In contrast, the highly aligned fiber-stacked structure of the A-TS membrane not only enabled more overall physical protection against dendrite penetration and provided more exposed active sites for the anchoring and activation of "dead" Li [59], but also ensured an even electric field distribution for homogeneous SEI formation and Li^+ diffusion; consequently, it exhibited a smooth surface with almost no dendrites (Figs. 4c and f and Fig. S11). In addition, a cycled A-TS@Li anode in a symmetric cell presented a smoother surface than C-TS@Li and bare Li anodes (Fig. S12), further demonstrating effective Li dendrite suppression by the A-TS membrane.

To gain more insights into the dendrite suppression mechanism via different protective layers, COMSOL Multiphysics software was used to simulate the electric field distribution when Li dendrites appear on the surface of the Li metal anode (Figs. 4g–i and Fig. S13). Without protection, Li ions are prone to gather around the formed dendrites due to the tip effect (Figs. 4g and j) [41,60]. In subsequent cycles, the charges focused around the dendrites will attract more Li ions, accelerating vertical dendrite growth until the battery short-circuits. Although the unevenly distributed electric field around Li dendrites can be dispersed by lithiophilic TS nanofibers, the tip effect still exists in the voids of crossed nanofibers (Figs. 4h and k). Owing to both the high lithiophilicity and the aligned fiber-stacked structure of the A-TS nanofibers, Li^+ tends to adsorb uniformly on the A-TS membrane and, in turn, induces homogeneous charge distribution on the surface of the Li anode (Figs. 4i and l), thus reducing the local current density of the Li anode and extending the Sand's time [61]. Moreover, homogeneous charge distribution can effectively prevent the tip effect and localized vertical growth of Li dendrites, contributing positively to smooth Li deposition and stripping during cycling.

The galvanostatic cycling performance of symmetric cells assembled with bare Li, C-TS@Li, and A-TS@Li anodes was assessed to further compare the stability of various anodes in repeated deposition/stripping processes (Fig. 5). At a current density of 0.5 mA cm^{-2} with a stripping/plating capacity of 0.5 mAh cm^{-2}, the bare Li exhibited an initial overpotential of 90.9 mV, much higher than the C-TS@Li (59.5 mV) and A-TS@Li (48.9 mV) electrodes (Fig. 5a). The polarization of the bare Li became unstable after 50 h, and the overpotential further increased to ~220 mV after 300 h. This polarization increase can be attributed to the gradual accumulation of "dead" Li on the surface of the Li metal, leading to

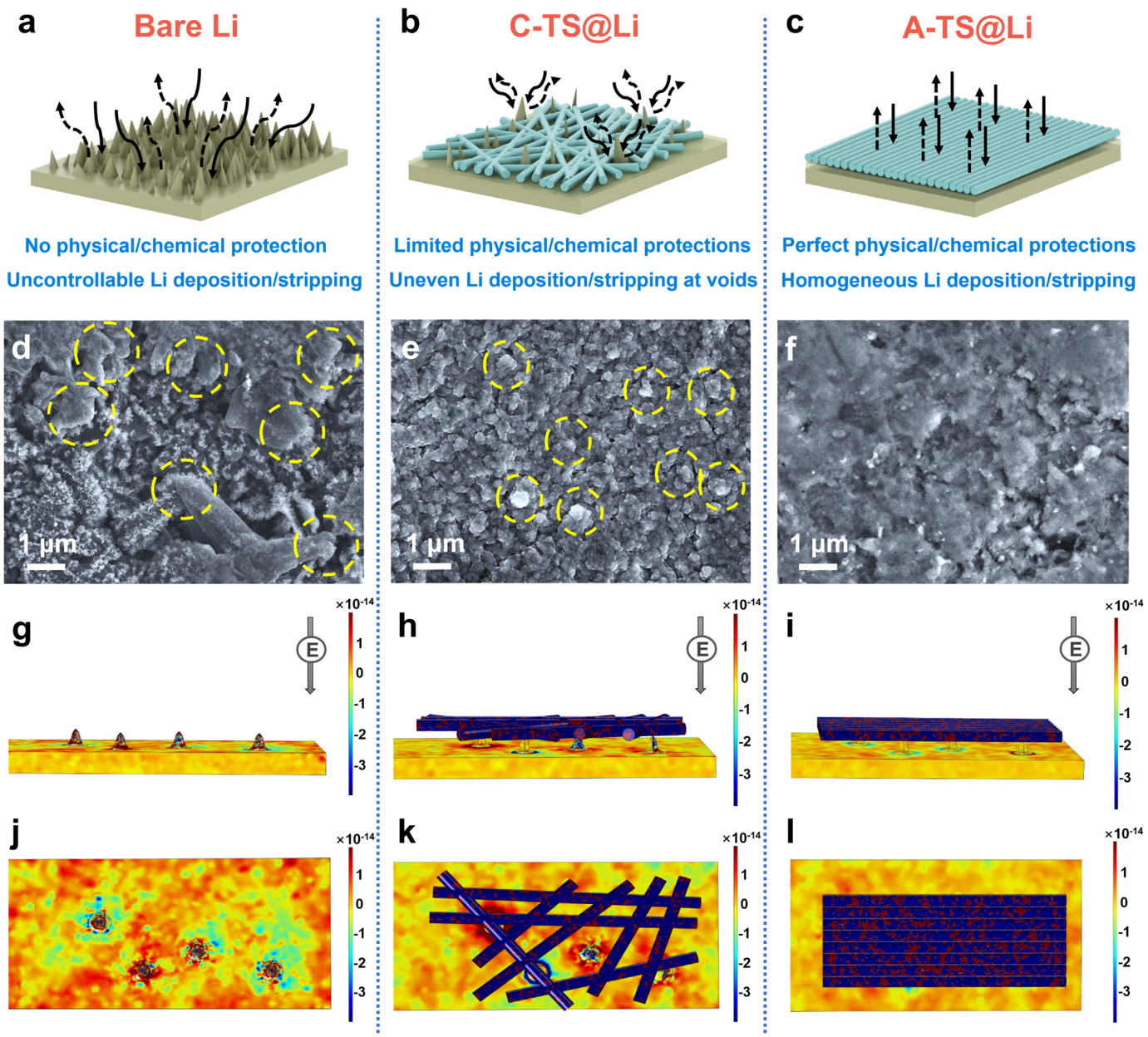

Fig. 4. Schematic illustrations of the Li deposition and stripping behaviors on the (a) bare Li, (b) C-TS@Li, and (c) A-TS@Li anodes; FE-SEM images of (d) the surface of the bare Li anode and the surfaces of the Li anodes with (e) C-TS and (f) A-TS membranes after 200 cycles in Li–S batteries; the finite element method using COMSOL Multiphysics to simulate the electric field distributions when Li dendrites grow on the (g and j) bare Li, (h and k) C-TS@Li, and (i and l) A-TS@Li anodes.

an aggravated Li/electrolyte interface and fragmentation of the SEI layer [62,63]. Despite the similar initial overpotential recorded for the C-TS@Li and A-TS@Li anodes, the highly aligned A-TS@Li facilitated smoother Li stripping/plating than C-TS@Li, judging by the lower polarization after 200 h. The A-TS@Li also exhibited the most stable polarization among the three tested anodes at a higher current density and when switching between low and high current densities (Fig. 5b), indicating excellent rate capability. Furthermore, the A-TS membrane maintained a stable voltage profile during the long-term stripping/plating cycles, even at a higher current density of 5 mA cm^{-2} (~73 mV after 300 h, in Figs. 5c and d). The same stability was observed for the A-TS@Li anode at a stripping/plating capacity as high as 5 mAh cm^{-2} (~35.4 mV after 300 h, in Figs. 5e and f, more stable than that of the bare Li, shown in Fig. S14).

To further demonstrate the significant role of the A-TS membrane in homogenizing Li deposition, it was used in a Li||A-TS@Cu cell. This cell delivered a high initial Coulombic efficiency of ~97% and remained at ~96% after 70 cycles at a current density of 1 mA cm^{-2} with a capacity of 1 mAh cm^{-2} (Fig. S15). All these results reflect that under the multiscale protection of the A-TS membrane, uniform deposition/stripping behaviors were well achieved for the Li metal anode.

Electrochemical impedance spectroscopic (EIS) and cyclic voltammetric (CV) analysis of Li–S full batteries provided more insights into the charge transfer mechanism of various anodes. Fig. 6a displays the EIS spectra of the bare Li, C-TS@Li, and A-TS@Li anodes at open-circuit voltage. The Nyquist plots of all three anodes constitute a high-frequency semicircle and a low-frequency sloped line, corresponding to the charge-transfer resistance (R_{ct}) and mass-diffusion process [64]. Based on the fitted equivalent electrical circuit model and the corresponding resistance data shown in the inset of Fig. 6a and in Table S1, the R_{ct} value of A-TS@Li (80.6 Ω) is lower than that of C-TS@Li (96.5 Ω) and bare Li (114.8 Ω). The lower charge-transfer resistance at A-TS@Li emphasizes the role of the lithiophilic membrane in easing charge

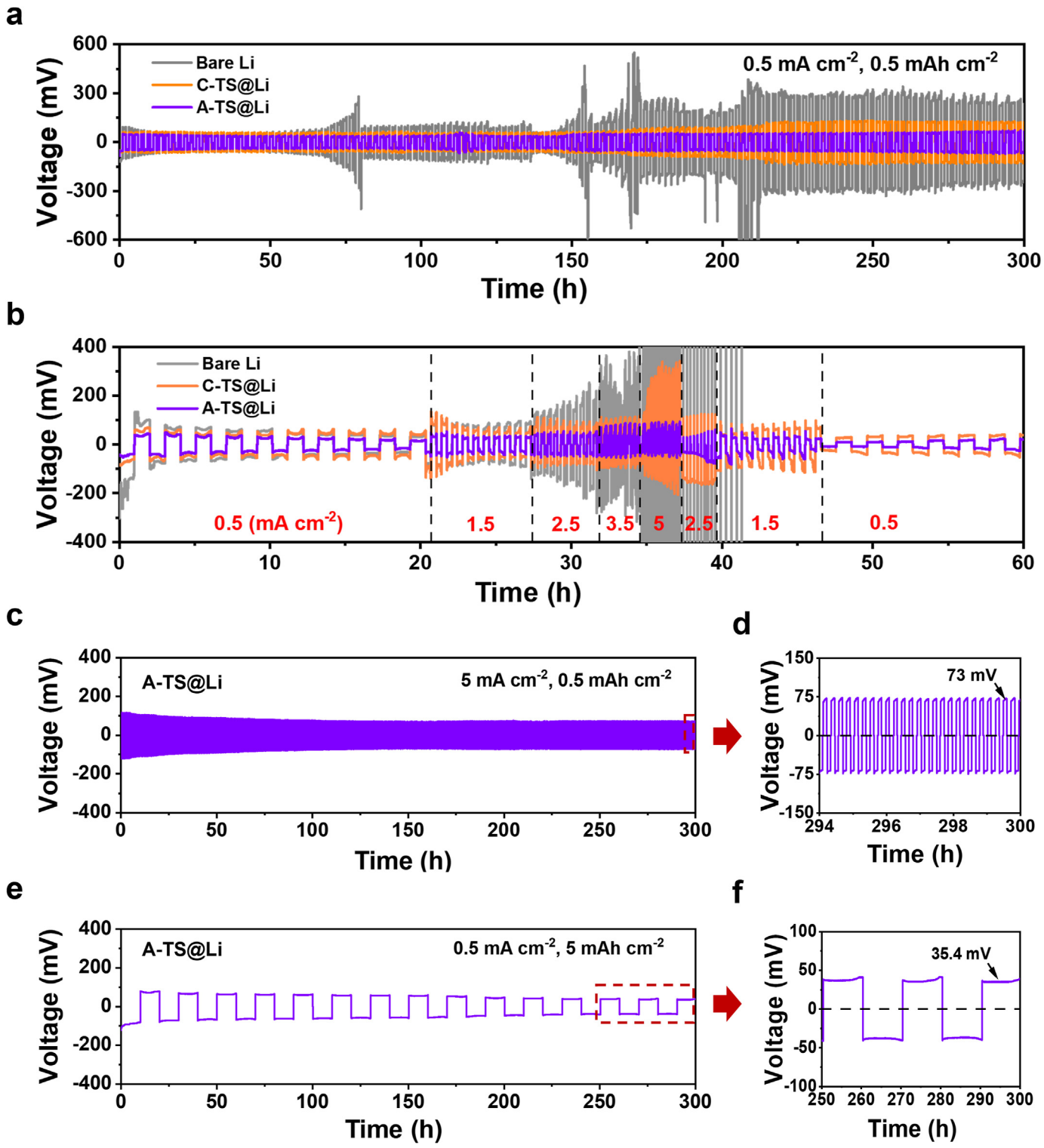

Fig. 5. (a) The voltage profiles of the symmetric cells assembled with bare Li, C-TS@Li, and A-TS@Li at 0.5 mA cm^{-2} with a stripping/plating capacity of 0.5 mAh cm^{-2}; (b) the rate performance of the symmetric cells assembled with bare Li, C-TS@Li, and A-TS@Li at a stripping/plating capacity of 0.5 mAh cm^{-2}; the voltage profiles of the symmetric cells assembled with A-TS@Li: (c, d) at 5 mA cm^{-2} with a stripping/plating capacity of 0.5 mAh cm^{-2} and (e, f) at 0.5 mA cm^{-2} with a stripping/plating capacity of 5 mAh cm^{-2}.

movement across the Li/electrolyte interface and speeding up the Faradaic reaction kinetics. The CVs recorded for the different anodes (bare Li, C-TS@Li, and A-TS@Li) at various scan rates ranging from 0.1 to 0.9 mV s^{-1} are illustrated in Fig. S16.

The Li diffusion coefficient (D_{Li^+}) in the three cases is calculated using the Randles–Sevcik equation to describe the Li diffusion process [65,66]. As can be seen from the CVs, all the cathodic current peaks ($I_{Peak\ A}$ and $I_{Peak\ B}$) and the anodic current peak ($I_{Peak\ C}$) show linear relationships with the square root of the scanning rate ($\nu^{0.5}$) of the three anodes, indicative of their diffusion-limited process [66]. Based on the calculated D_{Li^+} results (Fig. 6b and Table S2), Li^+ diffusion was faster on the A-TS@Li anode than on the bare Li and C-TS@Li anodes during both

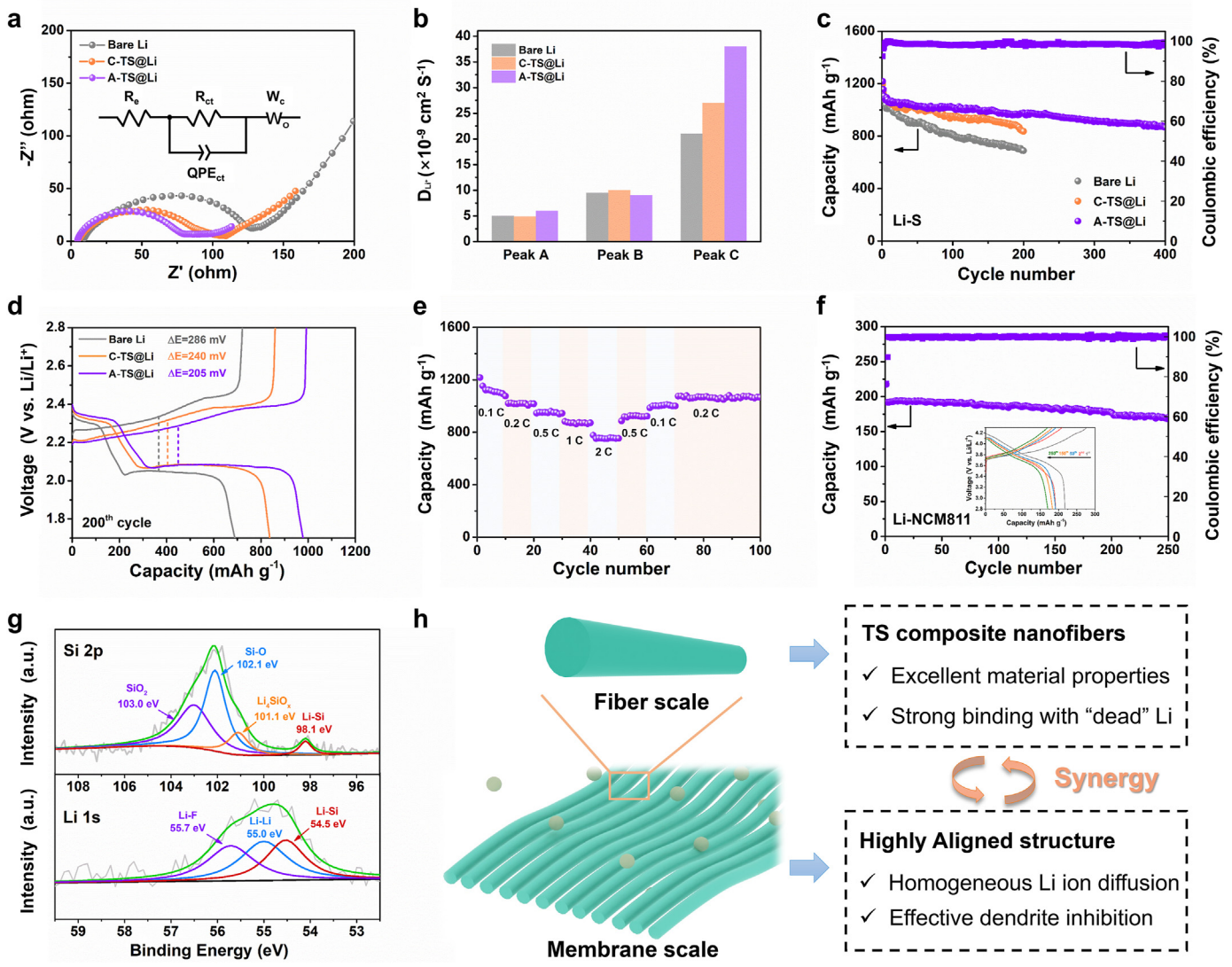

Fig. 6. (a) EIS curves of the Li–S batteries assembled with bare Li, C-TS@Li, and A-TS@Li, tested at open-circuit voltage; the inset is the equivalent circuit model; (b) values of CV peak current (I_p)/square root of the scan rates ($\nu^{0.5}$) for the bare Li, C-TS@Li, and A-TS@Li anodes in Li–S batteries in the first (peak A: $S_8 \rightarrow Li_2S_x$) and second (peak B: $Li_2S_x \rightarrow Li_2S_2/Li_2S$) cathodic reduction processes and the anodic oxidation process (peak C: $Li_2S_2/Li_2S \rightarrow S_8$); (c) long-term cycling performance of the Li–S batteries assembled with bare Li, C-TS@Li, and A-TS@Li at 0.2C with a potential window of 1.7–2.8 V (vs. Li/Li^+); (d) galvanostatic charge/discharge profiles of the bare Li, C-TS@Li, and A-TS@Li anodes at the 200th cycle at 0.2C; (e) rate performance of the Li–S batteries assembled with A-TS@Li from 0.1 to 2C; (f) long-term cycling performance of the Li||NCM811 batteries assembling with A-TS@Li at 0.5C with a potential window of 2.8–4.3 V (vs. Li/Li^+); the inset is the corresponding galvanostatic charge/discharge profile at different cycles; (g) high-resolution XPS spectra of Si 2p and Li 1s of the A-TS membrane's surface in the Li–S batteries assembled with A-TS@Li after 200 cycles; (h) schematic illustration of the multiscale functional superiority of the highly aligned TiO_2/SiO_2 electrospun nanofiber membrane in Li metal batteries.

reduction and oxidation. It should be mentioned here that for Li–S batteries, rapid Li^+ diffusion facilitates the sulfur transformation chemistry at the cathode side and enables efficient utilization of active sulfur for enhanced capacity performance [66,67,68].

The long-term cycling performance of various anodes in Li–S batteries is shown in Fig. 6c. The A-TS@Li anode delivered a high initial discharge capacity of 1218 mAh g^{-1} at 0.2C (1C = 1675 mAh g^{-1} in a Li–S battery), which remained stable at 869.5 mAh g^{-1} even after 400 cycles with a Coulombic efficiency of ~99% and a slow capacity attenuation (0.071% per cycle). Compared with a conventional Li–S battery, the weight increase in the whole cell was only 2.9% (Fig. S17). The galvanostatic charge/discharge profiles of the A-TS@Li anode (Fig. S18) also show stable discharge/charge characteristic voltage plateaus belonging to the Li–S battery from the 1st to the 400th cycle. In comparison, the capacity of the bare Li anode struggled with rapid capacity attenuation, reaching 689 mAh g^{-1} after 200 cycles. Although the C-TS@Li anode exhibited a high initial capacity of 1196.6 mAh g^{-1}, similar to the A-TS@Li anode, it could not maintain a stable cycling performance after 200 cycles. Furthermore, the A-TS@Li anode presented a lower polarization (205 mV) compared with the C-TS@Li (240 mV) and bare Li (286 mV) anodes (Fig. 6d), suggesting a lower energy barrier for the charge transfer process [64], in agreement with the EIS and diffusion coefficient results. The A-TS@Li anode also showed a stable rate performance, with the capacity decreasing to 756 mAh g^{-1} at 2C and recovering to 1066 mAh g^{-1} when the current density was reduced back to 0.1C (Fig. 6e and Fig. S19). This excellent performance by the A-TS@Li anode could be attributed to the lithiophilicity and nanofibrous array structure of the A-TS membrane, which helped achieve homogeneous charge transfer/diffusion and multiscale suppression of Li dendrite growth.

Motivated by the excellent performance of the A-TS@Li anode in Li–S batteries, we then tested the A-TS membrane in a Li metal battery system using an NCM811 ($LiNi_{0.8}Co_{0.1}Mn_{0.1}O_2$) cathode (Fig. 6f). The A-TS@Li

|| NCM811 battery achieved a stable discharge capacity of 187.2 mAh g^{-1} after 100 cycles at 0.5C. Batteries using C-TS@Li and bare Li anodes showed less stability, with the capacity decreasing after 100 cycles to 172.2 mAh g^{-1} and 162.5 mAh g^{-1}, respectively (Fig. S20). Even after continuous operation for 250 cycles, the battery with A-TS@Li retained a high capacity of 170.4 mAh g^{-1}. It should be mentioned here that this highly aligned protective layer outperformed any similar interlayer protection for the Li metal anode reported in the literature, as the data in Tables S3 and S4 and Fig. S21 show.

We further investigated the role of the A-TS membrane in suppressing dendrite growth on Li metal anodes via a series of post-mortem analyses after cycling in Li–S batteries. In addition to the surface morphological information from the cycled Li metal anodes, presented in Figs. 4d–f, the associated SEM images of the TS membrane are shown in Fig. S22, and the weight parameters of the Li anode and A-TS membrane before and after cycling are summarized in Table S5. After 200 cycles in Li–S batteries, the A-TS membrane enabled more effective anchoring of the "dead" Li than the C-TS membrane did. The high affinity of TS nanofibers toward Li and the more homogeneous Li^+ diffusion during the deposition/plating processes effectively controlled the "dead" Li deposition on the Li metals and prevented the vertical growth of Li dendrites caused by the tip effect. The fiber-stacked structure of the A-TS membrane provided more active sites to accommodate the "dead" Li (Fig. S23). The high-resolution XPS spectra of Si 2p and Li 1s for the cycled A-TS membrane are shown in Fig. 6g. Compared with the original TiO_2/SiO_2 composite, the A-TS nanofibers after cycling showed the peaks belonging to Li-containing compounds. In the Si 2p orbit, in addition to the peaks at 103.0 and 102.1 eV from the inherent SiO_2 compound in TS nanofibers, a Li_4SiO_x peak at 101.1 eV and a Li–Si peak at 98.1 eV were observed. Detection of Li–Si bonds confirmed that the electrochemical conversion and alloying reactions of SiO_2 played significant roles in binding with "dead" Li during cycling, as presented previously in Fig. 3 [69]. For the Li 1s orbit, the peak representing the Li–Si bond at 54.5 eV was again observed [69]. These results confirmed the effective electrochemical conversion of SiO_2 to Li_4SiO_x and of Si to Li–Si alloy. In addition, the Li–F bond at 55.7 eV may have derived from the formed SEI layer or the interaction between the anchored "dead" Li and the electrolyte [70,71].

Based on the above analysis, the functional mechanism of the A-TS membrane in the multiscale suppression of Li dendrite growth is summarized in Fig. 6h. At the fiber scale, introducing SiO_2 greatly enhances the mechanical properties of the TiO_2 electrospun nanofibers, allowing the formation of free-standing TS membranes as protective layers for the Li metal anode. The high chemical affinity of the TS nanofibers for Li attracts Li to attach to the nanofibers in the form of "dead" Li and then continuously reacts with the TS nanofibers. Consuming the Li on the TS nanofibers removes the pressure on the Li anode surface and prevents the vertical growth of Li dendrites. The TS composite nanofibers, with their high mechanical strength and thermal stability, physically resist being punctured by any formed dendrites and prevent the battery from short-circuiting if thermal runaway occurs. At the membrane scale, the special array structure composed of the highly aligned electrospun nanofibers achieves even charge distribution as well as homogeneous and fast Li^+ diffusion, removing the conditions that might favor dendrite seeding. The A-TS membrane also enables perfect physical protection to prevent rapid dendrite penetration through the membrane's large voids, as well as ensuring more exposed active sites for anchoring "dead" Li. Hence, stable deposition and stripping of the Li metal anode can be achieved under the protection of the A-TS membrane. However, to better optimize the electrochemical performance of A-TS membranes for future commercialization of Li–S batteries, the interaction between polysulfides and the A-TS membrane needs to be further investigated to reveal the mechanism by which the "shuttle effect" is suppressed. The introduction of flexible additives with high ionic conductivity may also be an effective method to broaden the application scope of the A-TS membrane.

3. Conclusion

In this work, we presented a highly aligned lithiophilic TiO_2/SiO_2 (A-TS) electrospun nanofiber membrane that can shield the Li metal anode from uncontrollable dendrite growth when used as a protective layer on the anode. This A-TS membrane was fabricated using an automatic fiber collection device and a specially designed electrospinning system. The highly aligned nanofibers controlled the structure of the membrane and prevented any large-scale voids, previously reported to allow some dendrite growth. With more control over the contact points between the protective layer and the Li metal, more homogeneous charge distribution was achieved, preventing local charge accumulation that might otherwise have induced dendrite growth. Our spectroscopic and DFT calculation results indicated that the individual TS nanofibers attracted more "dead" Li, with some evidence that Li reacted with the SiO_2 component in the fiber to form intermediate compounds containing Li–Si. Consuming some of the deposited Li in/on the TS fibers regulated the supply of Li^+ on the metal anode surface and significantly inhibited dendrite formation. As a result of the protective layer's multiple roles at both the membrane and the individual fiber level, dendrite formation was effectively suppressed, and the anode cycle life was significantly improved. In a Li–S system, applying the A-TS membrane allowed the cell to run for over 400 cycles with a capacity attenuation as low as 0.071% per cycle. In a Li metal system (with an NCM811 cathode), the A-TS@Li anode enabled the battery to maintain a high capacity of 170.4 mAh g^{-1} after 250 cycles. We therefore believe that this design concept of using a highly aligned lithiophilic nanofiber protective layer on the Li metal anode can provide more ideas for the future development of high-energy-density metal-based batteries such as Li/Na–S, Li/Na/Zn metal, and metal–air batteries.

Declaration of competing interest

The authors declare that they have no known competing financial interests or personal relationships that could have appeared to influence the work reported in this paper.

Acknowledgments

This work was supported by the National Natural Science Foundation of China (52172097), Key Research and Development Program of Shaanxi Province (2022GY-301), Zhejiang Provincial Natural Science Foundation of China (LGF21E020001), Fundamental Research Foundation for the Central Universities of China (xjh012020031) and China Scholarship Council foundation (201906285020). Qiong Cai would like to acknowledge the funding support from Faraday Institution LiSTAR Programme (EP/S003053/1, Grant FIRG014). The authors thank Zijun Ren of the Instrument Analysis Center of Xi'an Jiaotong University for assistance with SEM analysis, and thank the University of Surrey for access to its High Performance Computing facility and the Eureka HPC cluster.

Appendix A. Supplementary data

Supplementary data to this article can be found online at https://doi.org/10.1016/j.esci.2022.09.001.

References

[1] L. Zhou, T.-T. Zuo, C.Y. Kwok, S.Y. Kim, A. Assoud, Q. Zhang, J. Janek, L.F. Nazar, High areal capacity, long cycle life 4 V ceramic all-solid-state Li-ion batteries enabled by chloride solid electrolytes, Nat. Energy 7 (2022) 83–93.

[2] M. Liao, C. Wang, Y. Hong, Y. Zhang, X. Cheng, H. Sun, X. Huang, L. Ye, J. Wu, X. Shi, X. Kang, X. Zhou, J. Wang, P. Li, X. Sun, P. Chen, B. Wang, Y. Wang, Y. Xia, Y. Cheng, H. Peng, Industrial scale production of fibre batteries by a solution-extrusion method, Nat. Nanotechnol. 17 (2022) 372–377.

[3] Z. Zhang, Y. Li, R. Xu, W. Zhou, Y. Li, S.T. Oyakhire, Y. Wu, J. Xu, H. Wang, Z. Yu, D.T. Boyle, W. Huang, Y. Ye, H. Chen, J. Wan, Z. Bao, W. Chiu, Y. Cui, Capturing the swelling of solid-electrolyte interphase in lithium metal batteries, Science 375 (2022) 66–70.

[4] S. Zhang, S. Li, Y. Lu, Designing safer lithium-based batteries with nonflammable electrolytes: a review, eScience 1 (2021) 163–177.

[5] M.S. Kim, Z. Zhang, P.E. Rudnicki, Z. Yu, J. Wang, H. Wang, S.T. Oyakhire, Y. Chen, S.C. Kim, W. Zhang, D.T. Boyle, X. Kong, R. Xu, Z. Huang, W. Huang, S.F. Bent, L.W. Wang, J. Qin, Z. Bao, Y. Cui, Suspension electrolyte with modified Li^+ solvation environment for lithium metal batteries, Nat. Mater. 21 (2022) 445–454.

[6] X. Wang, R. Kerr, F. Chen, N. Goujon, J.M. Pringle, D. Mecerreyes, M. Forsyth, P.C. Howlett, Toward high-energy-density lithium metal batteries: opportunities and challenges for solid organic electrolytes, Adv. Mater. 32 (2020) 1905219.

[7] H. Li, D. Chao, B. Chen, X. Chen, C. Chuah, Y. Tang, Y. Jiao, M. Jaroniec, S.Z. Qiao, Revealing principles for design of lean-electrolyte lithium metal anode via in situ spectroscopy, J. Am. Chem. Soc. 142 (2020) 2012–2022.

[8] H. Zhang, L. Huang, H. Xu, X. Zhang, Z. Chen, C. Gao, C. Lu, Z. Liu, M. Jiang, G. Cui, A polymer electrolyte with a thermally induced interfacial ion-blocking function enables safety-enhanced lithium metal batteries, eScience 2 (2022) 201–208.

[9] X. Shen, R. Zhang, X. Chen, X.B. Cheng, X. Li, Q. Zhang, The failure of solid electrolyte interphase on Li metal anode: structural uniformity or mechanical strength? Adv. Energy Mater. 10 (2020) 1903645.

[10] X.Q. Zhang, T. Li, B.Q. Li, R. Zhang, P. Shi, C. Yan, J.Q. Huang, Q. Zhang, A sustainable solid electrolyte interphase for high-energy-density lithium metal batteries under practical conditions, Angew. Chem. Int. Ed. 59 (2020) 3252–3257.

[11] R. Wang, W. Cui, F. Chu, F. Wu, Lithium metal anodes: present and future, J. Energy Chem. 48 (2020) 145–159.

[12] Y.-G. Lee, S. Fujiki, C. Jung, N. Suzuki, N. Yashiro, R. Omoda, D.-S. Ko, T. Shiratsuchi, T. Sugimoto, S. Ryu, J.H. Ku, T. Watanabe, Y. Park, Y. Aihara, D. Im, I.T. Han, High-energy long-cycling all-solid-state lithium metal batteries enabled by silver-carbon composite anodes, Nat. Energy 5 (2020) 299–308.

[13] P. Jaumaux, Q. Liu, D. Zhou, X. Xu, T. Wang, Y. Wang, F. Kang, B. Li, G. Wang, Deep-eutectic-solvent-based self-healing polymer electrolyte for safe and long-life lithium-metal batteries, Angew. Chem. Int. Ed. 59 (2020) 9134–9142.

[14] X. Shen, R. Zhang, P. Shi, X. Chen, Q. Zhang, How does external pressure shape Li dendrites in Li metal batteries? Adv. Energy Mater. 11 (2021) 2003416.

[15] C.P. Yang, Y.X. Yin, S.F. Zhang, N.W. Li, Y.G. Guo, Accommodating lithium into 3D current collectors with a submicron skeleton towards long-life lithium metal anodes, Nat. Commun. 6 (2015) 8058.

[16] J. Wang, S. Yi, J. Liu, S. Sun, Y. Liu, D. Yang, K. Xi, G. Gao, A. Abdelkader, W. Yan, S. Ding, R.V. Kumar, Suppressing the shuttle effect and dendrite growth in lithium-sulfur batteries, ACS Nano 14 (2020) 9819–9831.

[17] Y. Liu, X. Xu, O.O. Kapitanova, P.V. Evdokimov, Z. Song, A. Matic, S. Xiong, Electro-chemo-mechanical modeling of artificial solid electrolyte interphase to enable uniform electrodeposition of lithium metal anodes, Adv. Energy Mater. (2022) 2103589.

[18] D. Lin, Y. Liu, Y. Cui, Reviving the lithium metal anode for high-energy batteries, Nat. Nanotechnol. 12 (2017) 194–206.

[19] Z. Ju, J. Nai, Y. Wang, T. Liu, J. Zheng, H. Yuan, O. Sheng, C. Jin, W. Zhang, Z. Jin, H. Tian, Y. Liu, X. Tao, Biomacromolecules enabled dendrite-free lithium metal battery and its origin revealed by cryo-electron microscopy, Nat. Commun. 11 (2020) 488.

[20] E. Cha, M.D. Patel, J. Park, J. Hwang, V. Prasad, K. Cho, W. Choi, 2D MoS_2 as an efficient protective layer for lithium metal anodes in high-performance Li-S batteries, Nat. Nanotechnol. 13 (2018) 337–344.

[21] Y. Zheng, S. Xia, F. Dong, H. Sun, Y. Pang, J. Yang, Y. Huang, S. Zheng, High performance Li metal anode enabled by robust covalent triazine framework-based protective layer, Adv. Funct. Mater. 31 (2020) 2006159.

[22] J. Tang, X. Peng, T. Lin, X. Huang, B. Luo, L. Wang, Confining ultrafine tin monophosphide in $Ti_3C_2T_x$ interlayers for rapid and stable sodium ion storage, eScience 1 (2021) 203–211.

[23] Q. Qin, N. Deng, L. Wang, L. Zhang, Y. Jia, Z. Dai, Y. Liu, W. Kang, B. Cheng, Novel flexible Mn-based carbon nanofiber films as interlayers for stable lithium-metal battery, Chem. Eng. J. 360 (2019) 900–911.

[24] Y. Lai, Y. Zhao, W. Cai, J. Song, Y. Jia, B. Ding, J. Yan, Constructing ionic gradient and lithiophilic interphase for high-rate Li-metal anode, Small 15 (2019) 1905171.

[25] M. Hu, Y. Yuan, Y. Liu, L. Tian, Y. Zhang, D. Long, Progressively providing ionic inhibitor via functional nanofiber layer to stabilize lithium metal anode, Electrochim. Acta 302 (2019) 301–309.

[26] J. Man, K. Liu, H. Zhang, Y. Du, J. Yin, X. Wang, J. Sun, Dendrite-free lithium metal anode enabled by ion/electron-conductive N-doped 3D carbon fiber interlayer, J. Power Sources 489 (2021) 229524.

[27] A.-L. Chen, N. Shang, Y. Ouyang, L. Mo, C. Zhou, W.W. Tjiu, F. Lai, Y.-E. Miao, T. Liu, Electroactive polymeric nanofibrous composite to drive in situ construction of lithiophilic SEI for stable lithium metal anodes, eScience 2 (2022) 192–200.

[28] Y. Chen, G. Zhou, W. Zong, Y. Ouyang, K. Chen, Y. Lv, Y.-E. Miao, T. Liu, Porous polymer composite separators with three-dimensional ion-selective nanochannels for high-performance Li-S batteries, Compos. Commun. 25 (2021) 100679.

[29] C. Zhou, W. Zong, G. Zhou, X. Fan, Y.-E. Miao, Radical-functionalized polymer nanofiber composite separator for ultra-stable dendritic-free lithium metal batteries, Compos. Commun. 25 (2021) 100696.

[30] J. Xue, T. Wu, Y. Dai, Y. Xia, Electrospinning and electrospun nanofibers: methods, materials, and applications, Chem. Rev. 119 (2019) 5298–5415.

[31] K. Wang, Y. Xu, H. Wu, R. Yuan, M. Zong, Y. Li, V. Dravid, W. Ai, J. Wu, A hybrid lithium storage mechanism of hard carbon enhances its performance as anodes for lithium-ion batteries, Carbon 178 (2021) 443–450.

[32] B.J. Landi, M.J. Ganter, C.D. Cress, R.A. DiLeo, R.P. Raffaelle, Carbon nanotubes for lithium ion batteries, Energy Environ. Sci. 2 (2009) 638–654.

[33] K. Lin, X. Qin, M. Liu, X. Xu, G. Liang, J. Wu, F. Kang, G. Chen, B. Li, Ultrafine titanium nitride sheath decorated carbon nanofiber network enabling stable lithium metal anodes, Adv. Funct. Mater. 29 (2019) 1903229.

[34] L. Yu, Q. Su, B. Li, L. Huang, G. Du, S. Ding, W. Zhao, M. Zhang, B. Xu, Pre-lithiated edge-enriched MoS_2 nanoplates embedded into carbon nanofibers as protective layers to stabilize Li metal anodes, Chem. Eng. J. 429 (2022) 132479.

[35] P. Xue, C. Sun, H. Li, J. Liang, C. Lai, Superlithiophilic amorphous SiO_2-TiO_2 distributed into porous carbon skeleton enabling uniform lithium deposition for stable lithium metal batteries, Adv. Sci. 6 (2019) 1900943.

[36] X. Li, Y. Zheng, Q. Pan, C.Y. Li, Polymerized ionic liquid-containing interpenetrating network solid polymer electrolytes for all-solid-state lithium metal batteries, ACS Appl. Mater. Interfaces 11 (2019) 34904–34912.

[37] J. Cui, S. Yao, M. Ihsan-Ul-Haq, J. Wu, J.-K. Kim, Correlation between li plating behavior and surface characteristics of carbon matrix toward stable Li metal anodes, Adv. Energy Mater. 9 (2019) 1802777.

[38] J. Wen, X. Song, X. Li, C. Yan, J. Zou, H. Wu, Q. Zhang, X. Zeng, Facile synthesis of hierarchical MoS_2/ZnS @ porous hollow carbon nanofibers for a stable Li metal anode, J. Colloid Interface Sci. 622 (2022) 347–356.

[39] T. Gu, J. Ren, S. Zhang, H. Guo, H. Wang, R.-P. Ren, Y.-K. Lv, Constructing MoS_2/ZnS-NC heterostructures on carbon cloth as anode with enhanced diffusion kinetics for lithium-ion batteries, J. Alloys Compd. 901 (2022) 163650.

[40] D. Wang, Y. Liu, X. Meng, Y. Wei, Y. Zhao, Q. Pang, G. Chen, Two-dimensional VS_2 monolayers as potential anode materials for lithium-ion batteries and beyond: first-principles calculations, J. Mater. Chem. 5 (2017) 21370–21377.

[41] X.B. Cheng, T.Z. Hou, R. Zhang, H.J. Peng, C.Z. Zhao, J.Q. Huang, Q. Zhang, Dendrite-free lithium deposition induced by uniformly distributed lithium ions for efficient lithium metal batteries, Adv. Mater. 28 (2016) 2888–2895.

[42] S. Xia, X. Zhang, C. Liang, Y. Yu, W. Liu, Stabilized lithium metal anode by an efficient coating for high-performance Li-S batteries, Energy Stor. Mater. 24 (2020) 329–335.

[43] A. Huang, Y. Ma, J. Peng, L. Li, S.-l. Chou, S. Ramakrishna, S. Peng, Tailoring the structure of silicon-based materials for lithium-ion batteries via electrospinning technology, eScience 1 (2021) 141–162.

[44] J. Wang, G. Yang, L. Wang, S. Wang, W. Yan, S. Ding, In-situ fabrication of transition-metal-doped TiO_2 nanofiber/nanosheet structure for high-performance Li storage, J. Alloys Compd. 787 (2019) 1110–1119.

[45] S.W. Yao, H.P. Kuo, Photocatalytic degradation of toluene on SiO_2/TiO_2 photocatalyst in a fluidized bed reactor, Procedia Eng. 102 (2015) 1254–1260.

[46] G. He, Y. Cai, Y. Zhao, X. Wang, C. Lai, M. Xi, Z. Zhu, H. Fong, Electrospun anatase-phase TiO_2 nanofibers with different morphological structures and specific surface areas, J. Colloid Interface Sci. 398 (2013) 103–111.

[47] Q. Zhang, J. Luan, D. Sun, Y. Tang, H. Wang, Plasma-treated Ti^{3+}-doped sodium titanate nanosheet arrays on titanium foil as a lithiophilic current collector for a stable lithium metal anode, Chem. Commun. 55 (2019) 6551–6554.

[48] L. Zhu, J. Wang, J. Liu, Z. Xu, M.S. Nasir, X. Chen, Z. Wang, S. Sun, Q. Ma, J. Liu, J. Feng, J. Liang, W. Yan, In situ enrichment amplification strategy enabling highly sensitive formaldehyde gas sensor, Sens. Actuator. B Chem. 354 (2022) 131206.

[49] Y. Jin, S. Li, A. Kushima, X. Zheng, Y. Sun, J. Xie, J. Sun, W. Xue, G. Zhou, J. Wu, F. Shi, R. Zhang, Z. Zhu, K. So, Y. Cui, J. Li, Self-healing SEI enables full-cell cycling of a silicon-majority anode with a coulombic efficiency exceeding 99.9, Energy Environ. Sci. 10 (2017) 580–592.

[50] J. Hu, Q. Wang, L. Fu, R. Rajagopalan, Y. Cui, H. Chen, H. Yuan, Y. Tang, H. Wang, Titanium monoxide-stabilized silicon nanoparticles with a litchi-like structure as an advanced anode for Li-ion batteries, ACS Appl. Mater. Interfaces 12 (2020) 48467–48475.

[51] K. Lin, X. Qin, M. Liu, X. Xu, G. Liang, J. Wu, F. Kang, G. Chen, B. Li, Ultrafine titanium nitride sheath decorated carbon nanofiber network enabling stable lithium metal anodes, Adv. Funct. Mater. 29 (2019) 1903229.

[52] K. Yan, Z. Lu, H.-W. Lee, F. Xiong, P.-C. Hsu, Y. Li, J. Zhao, S. Chu, Y. Cui, Selective deposition and stable encapsulation of lithium through heterogeneous seeded growth, Nat. Energy 1 (2016) 16010.

[53] P. Xue, C. Sun, H. Li, J. Liang, C. Lai, Superlithiophilic amorphous SiO_2–TiO_2 distributed into porous carbon skeleton enabling uniform lithium deposition for stable lithium metal batteries, Adv. Sci. 6 (2019) 1900943.

[54] R. Pathak, K. Chen, A. Gurung, K.M. Reza, B. Bahrami, F. Wu, A. Chaudhary, N. Ghimire, B. Zhou, W.H. Zhang, Y. Zhou, Q. Qiao, Ultrathin bilayer of graphite/SiO_2 as solid interface for reviving Li metal anode, Adv. Energy Mater. 9 (2019) 1901486.

[55] S.S. Zhang, X. Fan, C. Wang, Preventing lithium dendrite-related electrical shorting in rechargeable batteries by coating separator with a Li-killing additive, J. Mater. Chem. 6 (2018) 10755–10760.

[56] J.R. Szczech, S. Jin, Nanostructured silicon for high capacity lithium battery anodes, Energy Environ. Sci. 4 (2011) 56–72.

[57] C. Wu, F. Guo, L. Zhuang, X. Ai, F. Zhong, H. Yang, J. Qian, Mesoporous silica reinforced hybrid polymer artificial layer for high-energy and long-cycling lithium metal batteries, ACS Energy Lett. 5 (2020) 1644–1652.

[58] R. Xu, Y. Xiao, R. Zhang, X.B. Cheng, C.Z. Zhao, X.Q. Zhang, C. Yan, Q. Zhang, J.Q. Huang, Dual-phase single-ion pathway interfaces for robust lithium metal in working batteries, Adv. Mater. 31 (2019) 1808392.

[59] C. Fang, J. Li, M. Zhang, Y. Zhang, F. Yang, J.Z. Lee, M.H. Lee, J. Alvarado, M.A. Schroeder, Y. Yang, B. Lu, N. Williams, M. Ceja, L. Yang, M. Cai, J. Gu, K. Xu, X. Wang, Y.S. Meng, Quantifying inactive lithium in lithium metal batteries, Nature 572 (2019) 511–515.
[60] Y. Zhu, J. Xie, A. Pei, B. Liu, Y. Wu, D. Lin, J. Li, H. Wang, H. Chen, J. Xu, A. Yang, C.L. Wu, H. Wang, W. Chen, Y. Cui, Fast lithium growth and short circuit induced by localized-temperature hotspots in lithium batteries, Nat. Commun. 10 (2019) 2067.
[61] H.J.S. Sand, On the concentration at the electrodes in a solution, with special reference to the liberation of hydrogen by electrolysis of a mixture of copper sulphate and sulphuric acid, Philos. Mag. A 1 (1901) 45–79.
[62] H. Ye, Z.J. Zheng, H.R. Yao, S.C. Liu, T.T. Zuo, X.W. Wu, Y.X. Yin, N.W. Li, J.J. Gu, F.F. Cao, Y.G. Guo, Guiding uniform Li plating/stripping through lithium-aluminum alloying medium for long-life Li metal batteries, Angew. Chem. Int. Ed. 58 (2019) 1094–1099.
[63] Y. He, Z. Chang, S. Wu, Y. Qiao, S. Bai, K. Jiang, P. He, H. Zhou, Simultaneously inhibiting lithium dendrites growth and polysulfides shuttle by a flexible mof-based membrane in Li-S batteries, Adv. Energy Mater. 8 (2018) 1802130.
[64] J. Wang, G. Yang, J. Chen, Y. Liu, Y. Wang, C.Y. Lao, K. Xi, D. Yang, C.J. Harris, W. Yan, S. Ding, R.V. Kumar, Flexible and high-loading lithium-sulfur batteries enabled by integrated three-in-one fibrous membranes, Adv. Energy Mater. 9 (2019) 1902001.
[65] J. Liu, J. Wang, L. Zhu, X. Chen, Q. Ma, Z. Xu, S. Sun, N. Wang, Q. Chai, W. Yan, Hollow urchin-like Mn_3O_4 microspheres as an advanced sulfur host for enabling Li-S batteries with high gravimetric energy density, J. Colloid Interface Sci. 606 (2022) 1111–1119.
[66] G. Zhou, H. Tian, Y. Jin, X. Tao, B. Liu, R. Zhang, Z.W. Seh, D. Zhuo, Y. Liu, J. Sun, J. Zhao, C. Zu, D.S. Wu, Q. Zhang, Y. Cui, Catalytic oxidation of Li_2S on the surface of metal sulfides for li-s batteries, P. Natl. Acad. Sci. 114 (2017) 840–845.
[67] J. Liu, J. Wang, L. Zhu, X. Chen, Q. Ma, L. Wang, X. Wang, W. Yan, A high-safety and multifunctional MOFs modified aramid nanofiber separator for lithium-sulfur batteries, Chem. Eng. J. 411 (2021) 128540.
[68] J. He, A. Bhargav, A. Manthiram, High-energy-density, long-life lithium-sulfur batteries with practically necessary parameters enabled by low-cost Fe-Ni nanoalloy catalysts, ACS Nano 15 (2021) 8583–8591.
[69] J.Y. Kim, A.Y. Kim, G. Liu, J.Y. Woo, H. Kim, J.K. Lee, Li_4SiO_4-based artificial passivation thin film for improving interfacial stability of Li metal anodes, ACS Appl. Mater. Interfaces 10 (2018) 8692–8701.
[70] M. Zhou, Y. Lyu, Y. Liu, B. Guo, Porous scaffold of TiO_2 for dendrite-free lithium metal anode, J. Alloys Compd. 791 (2019) 364–370.
[71] J. Chen, X. Fan, Q. Li, H. Yang, M.R. Khoshi, Y. Xu, S. Hwang, L. Chen, X. Ji, C. Yang, H. He, C. Wang, E. Garfunkel, D. Su, O. Borodin, C. Wang, Electrolyte design for LiF-rich solid-electrolyte interfaces to enable high-performance microsized alloy anodes for batteries, Nat. Energy 5 (2020) 386–397.